Double-π fully scalable model for on-chip spiral inductors*

Liu Jun(刘军)[1,2], Zhong Lin(钟琳)[1], Wang Huang(王皇)[1], Wen Jincai(文进才)[1], Sun Lingling(孙玲玲)[1,†], Yu Zhiping(余志平)[1], and Marissa Condon[2]

[1]Key Laboratory of RF Circuits and Systems, Ministry of Education, Hangzhou Dianzi University, Hangzhou 310018, China
[2]School of Electronic Engineering, Dublin City University, Dublin 9, Ireland

Abstract: A novel double-π equivalent circuit model for on-chip spiral inductors is presented. A hierarchical structure, similar to that of MOS models is introduced. This enables a strict partition of the geometry scaling in the global model and the model equations in the local model. The major parasitic effects, including the skin effect, the proximity effect, the inductive and capacitive loss in the substrate, and the distributed effect, are analytically calculated with geometric and process parameters in the local-level. As accurate values of the layout and process parameters are difficult to obtain, a set of model parameters is introduced to correct the errors caused by using these given inaccurate layout and process parameters at the local level. Scaling rules are defined to enable the formation of models that describe the behavior of the inductors of a variety of geometric dimensions. A series of asymmetric inductors with different geometries are fabricated on a standard 0.18-μm SiGe BiCMOS process with 100 Ω/cm substrate resistivity to verify the proposed model. Excellent agreement has been obtained between the measured results and the proposed model over a wide frequency range.

Key words: spiral inductor; double-π equivalent circuit; fully scalable
DOI: 10.1088/1674-4926/33/8/084007 **EEACC:** 1310

1. Introduction

As a critical passive component, integrated spiral inductors have been widely used in CMOS RFIC design such as in RF amplifiers, voltage controlled oscillators (VCOs), mixers, filters and impedance matching circuits[1−5]. Therefore, an accurate equivalent circuit based model suitable for building a scalable spiral inductor library is essential for reliable circuit implementation and design optimization. Considerable research related to the modeling of on-chip spiral inductors has been published in recent years[6−19]. These methods are generally categorized into two types: numerical and compact circuit modeling techniques. Numerical techniques generally involve electromagnetic (EM) field solvers. Hence, they are time consuming. Therefore, Spice-format compact models (e.g. equivalent circuit models) are preferred by the IC designers.

Most of the research effort into equivalent circuit models of spiral inductors in the past years has focused on different topologies (such as the T model[6], single-π model[7−12], double-π model[13−19]) for accurate prediction of the characteristics of spiral inductors over a wide frequency range, for characterization of parasitic effects, for characterization of the capacitive and inductive coupling of the substrate, and on the model parameter extraction methods. Scalable models with scaling rules that be used to describe the behavior of spiral inductors over a whole geometric range are rarely presented.

In general, a scalable modeling procedure for inductors manufactured in a specified manufacture process is as follows. Firstly parameters are extracted for devices of various dimensions and secondly, a function is fitted to each parameter variation with the geometry. For scalable fitting, a unique parameter extraction solution and physically meaningful scaling expressions for each parameter are of the utmost importance to ensure the accuracy of the extracted scalable model. Among the reported parameter extraction approaches are the numerical optimization method, the analytic[11, 12, 16−18] and physical based[10, 13, 19] model parameter extraction techniques. The numerical optimization method is difficult to render scalable because the optimized parameters are not always unique. The availability of an analytic parameter extraction technique is strongly dependent on the complexity of the equivalent circuit used, e.g. whether every parameter can be directly determined from measurements or not. The errors introduced by the assumptions used to simplify the parameter extraction at high frequencies tend to hinder the scalability of the models. On the contrary, physically-based model parameter extraction methods are expected to be unique, because of the strictly defined calculation method based on the layout and process parameters.

Double-π type models have been widely employed in building model libraries to achieve wideband accuracy. Two different scalable models for inductors are developed in Refs. [13, 20]. In Ref. [13], a set of complicated functions are utilized to calculate C_{ox}, C_{si} and C_p, making the parameter-extraction procedure and scalable rules intricate. The analytic parameter extraction methodology is developed in Ref. [20]. In this way, rules are arbitrary, multi-value phenomenon for parameters is more serious, and the errors of scaling rules for non-sampling geometries are hard to control. In this paper, a physics-based scalable modeling method for on-chip spiral inductors is proposed. The data included in the study cover the range from 0.1 to 22 nH, a total of 90 spiral inductors. The proposed scalable rules well reflect local level scaling of the

* Project supported by the State Key Development Program for Basic Research of China (No. 2010CB327403).
† Corresponding author. Email: sunll@hdu.edu.cn
Received 10 February 2012, revised manuscript received 18 March 2012

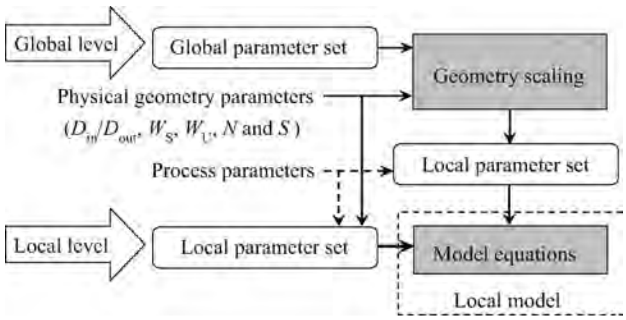

Fig. 1. Simplified schematic overview of the proposed model's hierarchical structure.

various component parameters. The proposed scaling rules and modeling method has strong practicality and reference, which has not been reported in previous works. The major parasitic effects, including the skin effect, the proximity effect, the vertical and lateral high frequency losses in the substrate and the distributed effect are analytically calculated with layout and process parameters. By using the complex effective thickness of the substrate that the eddy current is flowing through, novel equations for the high frequency lateral substrate losses are proposed. The overall double-π equivalent circuit with scalable rules is firstly given in Section II. As the scaling rules for the model components are physics based, compare with the experimentally scaled double-π model we presented early[20], the model parameter extraction becomes more clear and easier than the old model. Results from the presented model and measurements of spiral inductors fabricated on a standard 0.18 μm SiGe BiCMOS process are compared in Section 3. Finally, conclusions are drawn in Section 4.

2. Physics-based double-π equivalent circuit model and model parameter extraction method

2.1. Model structure

The proposed spiral inductor model has a hierarchical structure, which is similar to that of standard transistor models such as BSIM3v3.2 and PSP. A strict separation of the geometry scaling in the global model and the model equations in the local model is introduced. Consequently, the model can be used at either one of the two levels. The described model structure is schematically depicted in Fig. 1.

2.2. Model topology

The topology of the proposed double-π equivalent circuit model is shown in Fig. 3. In the circuit, L_{si} and $R_{si}\,(i = 1, 2)$ are the DC inductance and resistance, respectively. The L_{spij}–$R_{spij}\,(i = 1, 2;\ j = 1, 2, 3)$ ladders with the mutual inductors M_{i12}, M_{i13}, and M_{i23}, $(i = 1, 2)$ are used to capture the skin and proximity effects. C_p is the forward capacitance, which includes the overlap capacitance C_{mu} and the coupling capacitance C_{mm} between the neighboring turns. $C_{oxij}\,(i = 1, 2;\ j = 1, 2)$ represents the oxide-capacitance between the inductor and the substrate[7]. R_{subij} and C_{subij} $(i = 1, 2;\ j = 1, 2)$ are the vertical substrate resistance and capacitance of the substrate,

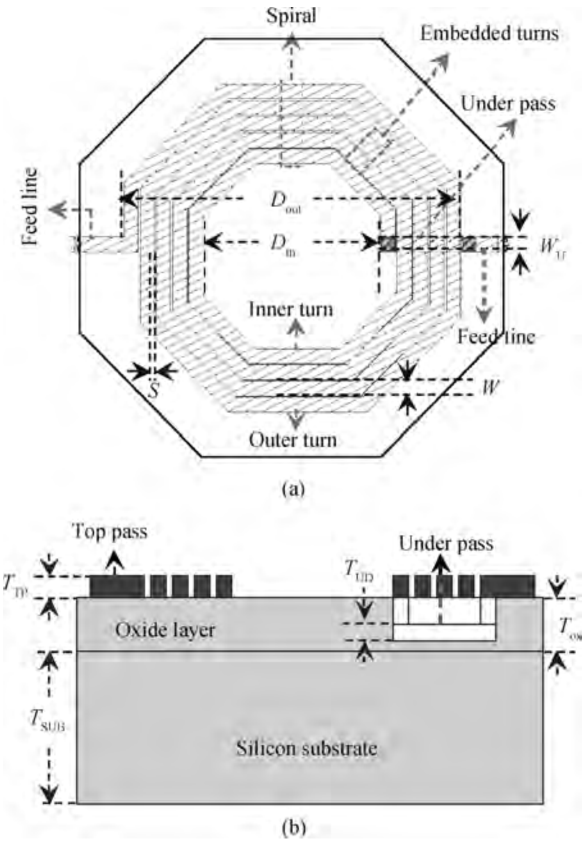

Fig. 2. (a) Top view of an octangular inductor. (b) Cross-section view of an on-chip spiral inductor. The definition of the geometry parameters as given in Tables 1 and 2 are illustrated. As seen from the Fig. 2(a), an inductor with a given shape can be completely specified by the number of turners N, the spiral turn width W_S, the under-pass width W_U, the turn spacing S, and any one of the following: the inner diameter D_{in} or the outer diameter D_{out}.

Table 1. Physical geometry parameters.

Name	Default	Description
D_{in}/D_{out} (μm)	60	Inner/Outer diameter
W_S (μm)	10	Width of spiral turn
W_U (μm)	10	Width of underpass
N	2.5	Number of turns
S (μm)	2	Turns spacing

respectively. $R_{loss\,j}$ and $L_{loss\,j}$ $(j = 1, 2)$ are introduced to represent the lateral resistive and inductive losses caused by the eddy current in the substrate.

2.3. Model parameters

As accurate values of the layout and process parameters are difficult to obtain, a set of model parameters is introduced to correct the errors caused by using these given inaccurate layout and process parameters at the local level. For one specific instance of an inductor, a local parameter set is internally generated using the relevant geometric (as given in Table 1) and process parameters (as given in Table 2). The local parameter set gives a complete and accurate description of the electrical properties of a specific device with a particular geometry.

Since most of these local parameters scale with geometry,

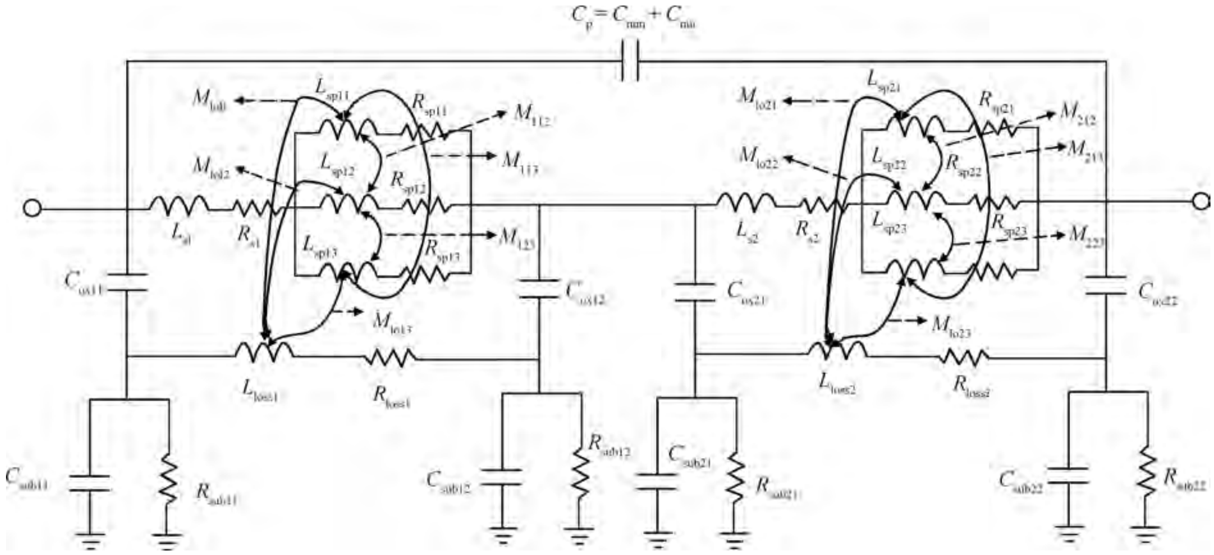

Fig. 3. Proposed double-π quivalent circuit model for asymmetric spiral inductors.

Table 2. Process parameters.

Name	Default	Description
R_{TP} (Ω/□)	0.015	Sheet resistance of spiral
T_{TP} (μm)	2.9	Thickness of spiral
R_{UD} (Ω/□)	0.028	Sheet resistance of underpass
T_{UD} (μm)	0.85	Thickness of underpass
C_{MU} (μF/m^2)	34.2	Spiral to underpass capacitance
C_{MUF} (pF/m)	21	Spiral to underpass fringing capacitance
C_{MM} (pF/m)	89.8	Spiral turn to turn capacitance
C_{MS} (μF/m^2)	4.307	Spiral to substrate capacitance
C_{MSF} (pF/m)	3.91	Spiral to substrate fringing capacitance
C_{MMSF} (pF/m)	2.3	Metal windings to substrate fringing capacitance for embedded lines
C_{US} (μF/m^2)	5.357	Underpass to substrate capacitance
C_{USF} (pF/m)	6.25	Underpass to substrate fringing capacitance
T_{SUB} (μm)	700	Substrate thickness
R_{SUB} (Ω·cm)	100	Substrate resistivity
T_{OX} (μm)	6.664	Oxide layer thickness

all inductors of a particular process can be described by a set of parameters, called the global parameter set. A set of scaling rules relates the local and global parameter set. By applying the set of scaling rules, a local parameter set can be obtained from a global parameter set. An overview of the local and global parameters in the model is given in the first and second column of Table 3.

2.4. Model equations for local level

As seen from Fig. 3, there are more than 22 elements in each single-π topology, giving a total of 45 elements for the proposed double-π equivalent model. To the best of the authors' knowledge, it is hard to extract such a model by analytic parameter extraction techniques or by the method proposed in Ref. [16], which employs simple single-π model parameters to determine a double-π model. Physics-based equations are carefully investigated and employed for the local model determination in this section. The set of local parameters are employed in the equations for correction of the errors arising from inaccurate process and layout parameters.

The model equations for all of the elements depicted in Fig. 3 are given as follows.

2.4.1. Skin and proximity effects model: L_{spij}, R_{spij} and mutual inductances, M_{i12}, M_{i13}, and M_{i23}, ($i = 1, 2$; $j = 1, 2, 3$)

With an increase in the frequency, the skin effect causes current crowding towards the surface of the conductor. The current density decreases from the surface to the center of the conductor. If the cross-section of the conductor is partitioned into many smaller subsections (in this work, three subsections are used), the current distribution in each subsection can be taken as uniform[21]. A simplified partitioning and modeling method as seen in Fig. 4 is used to accurately capture the skin and proximity effects. The thickness and width for the partitioned three subsections of a metal line with a thickness T_h, width W_i, and length l_e are defined as h_{1s}, h_{2s} and h_{3s}, and w_{1s}, w_{2s} and w_{3s}, respectively.

At the frequency f_{max} (the highest frequency used in this work is 20 GHz), the skin depth of metal winding line, δ_{max} can be calculated as

$$\delta_{max} = \sqrt{\frac{1}{\pi f_{max} \mu \sigma_m}}, \tag{1}$$

where μ and σ_m are the permeability and conductivity of metal line, respectively. σ_m is defined as

$$\sigma_m = \left(R_{\square} T_h\right)^{-1}, \tag{2}$$

where $R_{\square}$ is the metal sheet resistivity.

In this work, experimental relationships between h_{js} (j = 1, 2, 3) and δ_{max} defined as given in Eqs. (3)–(5) are used to determine the thicknesses (h_{1s}, h_{2s} and h_{3s}) of the three subsections, respectively.

Table 3. Model parameter set and the geometry scaling rules. A total of 17 local parameters and 68 global model parameters are used for asymmetric on-chip spiral inductors. Extracted results of the global parameter set for devices listed in Table 4 are given.

Local parameter set	Global parameter set	Geometry scaling for local parameter set	Extracted results of the global parameter set for devices listed in Table 4
l_{spcorr}	$l_{\text{sp1}}, l_{\text{sp2}}, l_{\text{sp3}}, l_{\text{sp4}}$	$l_{\text{spcorr}} = l_{\text{sp1}} h_{\text{p}}^{l_{\text{sp2}}} N^{l_{\text{sp3}}} D_{\text{in}}^{l_{\text{sp4}}}$	0.7945, −0.9205, 0.6433, 0.3471
r_{spcorr}	$r_{\text{sp1}}, r_{\text{sp2}}, r_{\text{sp3}}, r_{\text{sp4}}$	$r_{\text{spcorr}} = r_{\text{sp1}} h_{\text{p}}^{r_{\text{sp2}}} N^{r_{\text{sp3}}} D_{\text{in}}^{r_{\text{sp4}}}$	0.0218, −1.368, −0.1977, 0.0967
c_{pcorr}	$c_{\text{p1}}, c_{\text{p2}}, c_{\text{p3}}, c_{\text{p4}}$	$c_{\text{pcorr}} = c_{\text{p1}} h_{\text{p}}^{c_{\text{p2}}} N^{c_{\text{p3}}} D_{\text{in}}^{\text{cp4}}$	1.438, −0.9049, −1.299, 0.1428
c_{oxcorr11}	$c_{\text{ox11}}, c_{\text{ox12}}, c_{\text{ox13}}, c_{\text{ox14}}, c_{\text{ox15}}$	$c_{\text{oxcorr11}} = c_{\text{ox11}} h_{\text{p}}^{c_{\text{ox12}}} N^{c_{\text{ox13}}} D_{\text{in}}^{c_{\text{ox14}}} W_{\text{S}}^{c_{\text{ox15}}}$	0.005237, −0.5084, −0.3639, 0.215, −0.562
c_{oxcorr12}	$c_{\text{ox121}}, c_{\text{ox122}}, c_{\text{ox123}}, c_{\text{ox124}}, c_{\text{ox125}}$	$c_{\text{oxcorr12}} = c_{\text{ox121}} h_{\text{p}}^{c_{\text{ox122}}} N^{c_{\text{ox123}}} D_{\text{in}}^{c_{\text{ox124}}} W_{\text{S}}^{c_{\text{ox125}}}$	0.2437, −0.2584, −0.7202, 0.05421, −0.05775
c_{oxcorr22}	$c_{\text{ox21}}, c_{\text{ox22}}, c_{\text{ox23}}, c_{\text{ox24}}, c_{\text{ox25}}$	$c_{\text{oxcorr22}} = c_{\text{ox21}} h_{\text{p}}^{c_{\text{ox22}}} N^{c_{\text{ox23}}} D_{\text{in}}^{c_{\text{ox24}}} W_{\text{S}}^{c_{\text{ox25}}}$	0.001061, 0.1896, −0.3967, 0.1706, −0.6638
$c_{\text{subcorr11}}$	$c_{\text{sub11}}, c_{\text{sub12}}, c_{\text{sub13}}, c_{\text{sub14}}$	$c_{\text{subcorr11}} = c_{\text{sub11}} h_{\text{p}}^{c_{\text{sub12}}} N^{c_{\text{sub13}}} D_{\text{in}}^{c_{\text{sub14}}}$	15.74, 0.4367, −0.6414, 0.2686
$c_{\text{subcorr12}}$	$c_{\text{sub121}}, c_{\text{sub122}}, c_{\text{sub123}}, c_{\text{sub124}}$	$c_{\text{subcorr12}} = c_{\text{sub121}} h_{\text{p}}^{c_{\text{sub122}}} N^{c_{\text{sub123}}} D_{\text{in}}^{c_{\text{sub124}}}$	0.003289, 1.031, −1.298, −0.8483
$c_{\text{sbucorr22}}$	$c_{\text{sub21}}, c_{\text{sub22}}, c_{\text{sub23}}, c_{\text{sub24}}$	$c_{\text{subcorr22}} = c_{\text{sub21}} h_{\text{p}}^{c_{\text{sub22}}} N^{c_{\text{sub23}}} D_{\text{in}}^{c_{\text{sub24}}}$	9.295, 0.7762, −0.8756, 0.1861
$r_{\text{subcorr11}}$	$r_{\text{sub11}}, r_{\text{sub12}}, r_{\text{sub13}}, r_{\text{sub14}}$	$r_{\text{subcorr11}} = r_{\text{sub11}} h_{\text{p}}^{r_{\text{sub12}}} N^{r_{\text{sub13}}} D_{\text{in}}^{r_{\text{sub14}}}$	32.76, −0.5752, 1.71, 0.7687
$r_{\text{subcorr12}}$	$r_{\text{sub121}}, r_{\text{sub122}}, r_{\text{sub123}}, r_{\text{sub124}}$	$r_{\text{subcorr12}} = r_{\text{sub121}} h_{\text{p}}^{r_{\text{sub122}}} N^{r_{\text{sub123}}} D_{\text{in}}^{r_{\text{sub124}}}$	12.69, −0.8495, 0.3311, 0.3437
$r_{\text{sbucorr22}}$	$r_{\text{sub21}}, r_{\text{sub22}}, r_{\text{sub23}}, r_{\text{sub24}}$	$r_{\text{subcorr22}} = r_{\text{sub21}} h_{\text{p}}^{r_{\text{sub22}}} N^{r_{\text{sub23}}} D_{\text{in}}^{r_{\text{sub24}}}$	5.058, 0.4124, 1.715, 0.5148
$r_{\text{losscorr1}}$	$r_{\text{lo11}}, r_{\text{lo12}}, r_{\text{lo13}}, r_{\text{lo14}}$	$r_{\text{losscorr1}} = r_{\text{lo11}} h_{\text{p}}^{r_{\text{lo12}}} N^{r_{\text{lo13}}} D_{\text{in}}^{r_{\text{lo14}}}$	4.23, −0.036, 0.35, 0.08537
$r_{\text{losscorr2}}$	$r_{\text{lo21}}, r_{\text{lo22}}, r_{\text{lo23}}, r_{\text{lo24}}$	$r_{\text{losscorr2}} = r_{\text{lo21}} h_{\text{p}}^{r_{\text{lo22}}} N^{r_{\text{lo23}}} D_{\text{in}}^{r_{\text{lo24}}}$	4.36, −0.03455, 0.3547, 0.089
$l_{\text{losscorr1}}$	$l_{\text{lo11}}, l_{\text{lo12}}, l_{\text{lo13}}, l_{\text{lo14}}$	$l_{\text{losscorr1}} = l_{\text{lo11}} h_{\text{p}}^{l_{\text{lo12}}} N^{l_{\text{lo13}}} D_{\text{in}}^{l_{\text{lo14}}}$	1.737, −0.4737, 0.262, 0.1918
$l_{\text{losscorr2}}$	$l_{\text{lo21}}, l_{\text{lo22}}, l_{\text{lo23}}, l_{\text{lo24}}$	$l_{\text{losscorr2}} = l_{\text{lo21}} h_{\text{p}}^{l_{\text{lo22}}} N^{l_{\text{lo23}}} D_{\text{in}}^{l_{\text{lo24}}}$	1.642, −0.4776, 0.256, 0.1854
r_{dccorr}	$rl_{\text{dc1}}, r_{\text{dc2}}, r_{\text{dc3}}, r_{\text{dc4}}$	$r_{\text{dccorr}} = r_{\text{dc1}} h_{\text{p}}^{r_{\text{dc2}}} N^{r_{\text{dc3}}} D_{\text{in}}^{r_{\text{dc4}}}$	1.474, −0.2628, −0.1162, 0.03109
l_{dccorr}	$l_{\text{dc1}}, l_{\text{dc2}}, l_{\text{dc3}}, l_{\text{dc4}}$	$l_{\text{dccorr}} = l_{\text{dc1}} h_{\text{p}}^{l_{\text{dc2}}} N^{l_{\text{dc3}}} D_{\text{in}}^{l_{\text{dc4}}}$	0.2788, 0.2942, −0.03423, −0.1537

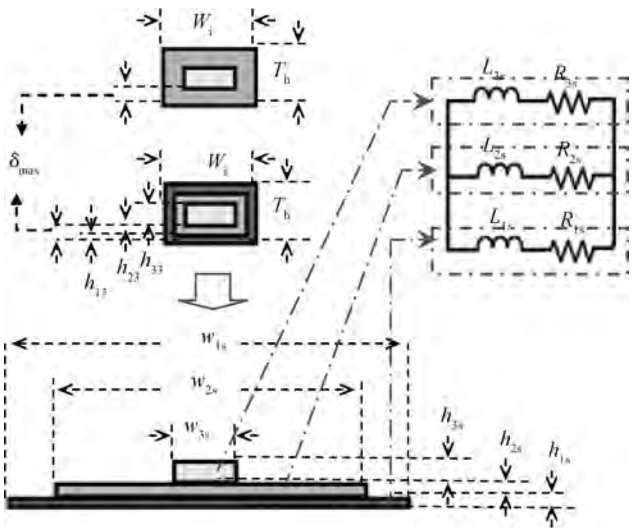

Fig. 4. Schematic of the skin effect modeling method.

$$h_{1s} = \delta_{max}/3, \tag{3}$$

$$h_{2s} = 2\delta_{max}/3, \tag{4}$$

$$h_{3s} = T_h - 2\delta_{max}. \tag{5}$$

Figure 4 depicts the cross section of the metal winding shown in Fig. 2. The metal winding is divided into three layers according the skin depth. Once h_{1s}, h_{2s} and h_{3s} are known, the width of the three layers of the metal winding can be calculated by unfolding the three layers as shown in Fig. 4.

$$w_{1s} = 2\left(W_i + T_h - 2h_{1s}\right), \tag{6}$$

$$w_{2s} = 2\left(W_i + T_h - 4h_{1s} - 2h_{2s}\right), \tag{7}$$

$$w_{3s} = W_i - 2\delta_{max}. \tag{8}$$

By applying the DC resistance and self-inductance calculation method[22] to rectangular conductors, the six equivalent circuit model parameters as shown in the upper right corner of Fig. 4, R_{1s}, R_{2s}, R_{3s}, L_{1s}, L_{2s} and L_{3s} can be determined as follows:

$$R_{js} = \frac{1}{\sigma_m}\frac{l_e}{h_{js}w_{js}}, \quad j = 1, 2, 3, \tag{9}$$

$$L_{js} = 2l_e\left(\lg\frac{2l_e}{w_{js}+h_{js}} + 0.50049 + \frac{w_{js}+h_{js}}{3l_e}\right)\cdot 10^{-7}, \quad j = 1, 2, 3. \tag{10}$$

The equivalent radius of the three subsections is given by

$$\text{rad}_{1s} = 0.2235\left(W_i + T_h\right)/0.7788, \tag{11}$$

$$\text{rad}_{2s} = 0.2235\left(W_i + T_h - 4h_{1s}\right)/0.7788, \tag{12}$$

$$\text{rad}_{3s} = 0.2235\left[W_i + T_h - 4\left(h_{1s} + h_{2s}\right)\right]/0.7788. \tag{13}$$

The geometric mean distance gmd_{12s}, gmd_{13s}, and gmd_{23s} between the three parts are given by

$$\text{gmd}_{12s} = \exp\left[\frac{\text{rad}_{1s}^2\cdot\ln\left(\text{rad}_{1s}\right) - \text{rad}_{2s}^2\cdot\ln\left(\text{rad}_{2s}\right)}{\text{rad}_{1s}^2 - \text{rad}_{2s}^2} - 0.5\right], \tag{14}$$

$$\text{gmd}_{13s} = \exp\left[\frac{\text{rad}_{1s}^2\cdot\ln\left(\text{rad}_{1s}\right) - \text{rad}_{3s}^2\cdot\ln\left(\text{rad}_{3s}\right)}{\text{rad}_{1s}^2 - \text{rad}_{3s}^2} - 0.5\right], \tag{15}$$

$$\text{gmd}_{23s} = \exp\left[\frac{\text{rad}_{2s}^2\cdot\ln\left(\text{rad}_{2s}\right) - \text{rad}_{3s}^2\cdot\ln\left(\text{rad}_{3s}\right)}{\text{rad}_{2s}^2 - \text{rad}_{3s}^2} - 0.5\right]. \tag{16}$$

The mutual inductance between the three parts is,

$$M_{12\mathrm{s}} = 2l_{\mathrm{e}}\left[\ln\left(\frac{l_{\mathrm{e}}}{\mathrm{gmd}_{12\mathrm{s}}} + \sqrt{1+\frac{l_{\mathrm{e}}^2}{\mathrm{gmd}_{12\mathrm{s}}^2}}\right) - \sqrt{1+\frac{\mathrm{gmd}_{12\mathrm{s}}^2}{l_{\mathrm{e}}^2}} + \frac{\mathrm{gmd}_{12\mathrm{s}}}{l_{\mathrm{e}}}\right]\cdot 10^{-7}, \tag{17}$$

$$M_{13\mathrm{s}} = 2l_{\mathrm{e}}\left[\ln\left(\frac{l_{\mathrm{e}}}{\mathrm{gmd}_{13\mathrm{s}}} + \sqrt{1+\frac{l_{\mathrm{e}}^2}{\mathrm{gmd}_{13\mathrm{s}}^2}}\right) - \sqrt{1+\frac{\mathrm{gmd}_{13\mathrm{s}}^2}{l_{\mathrm{e}}^2}} + \frac{\mathrm{gmd}_{13\mathrm{s}}}{l_{\mathrm{e}}}\right]\cdot 10^{-7}, \tag{18}$$

$$M_{23\mathrm{s}} = 2l_{\mathrm{e}}\left[\ln\left(\frac{l_{\mathrm{e}}}{\mathrm{gmd}_{23\mathrm{s}}} + \sqrt{1+\frac{l_{\mathrm{e}}^2}{\mathrm{gmd}_{23\mathrm{s}}^2}}\right) - \sqrt{1+\frac{\mathrm{gmd}_{23\mathrm{s}}^2}{l_{\mathrm{e}}^2}} + \frac{\mathrm{gmd}_{23\mathrm{s}}}{l_{\mathrm{e}}}\right]\cdot 10^{-7}. \tag{19}$$

So following this approach, the metal segments used in a spiral inductor can be divided into three segments: the spiral, which has the length of l_{m}, the feed line, which has the length of l_{fd}, and the underpass, which has the length of l_{up}, respectively. In this work, the width of feed line equals to that of the metal winding lines. $R_{\square}$, T_{h}, W_{i} and l_{e} are replaced with R_{TP}, T_{TP}, W_{S}, the total length of the spiral, l_{total} for the spiral and with R_{UD}, T_{UD}, W_{U}, l_{up}, for the underpass. L_{spij} and R_{spij} can be determined by using Eqs. (1)–(10), respectively, as follows,

$$R_{\mathrm{sp}ij} = \frac{1}{2}r_{\mathrm{spcorr}}(R_{\mathrm{w}j} + R_{\mathrm{u}j}),\quad i = 1,2;\ j = 1,2,3, \tag{20}$$

$$L_{\mathrm{sp}ij} = \frac{1}{2}l_{\mathrm{spcorr}}(L_{\mathrm{w}j} + L_{\mathrm{u}j}),\quad i = 1,2;\ j = 1,2,3, \tag{21}$$

$$M_{i12} = M_{12\mathrm{w}} + M_{12\mathrm{u}},\quad i = 1,2, \tag{22}$$

$$M_{i13} = M_{13\mathrm{w}} + M_{13\mathrm{u}},\quad i = 1,2, \tag{23}$$

$$M_{i23} = M_{23\mathrm{w}} + M_{23\mathrm{u}},\quad i = 1,2, \tag{24}$$

where r_{spcorr} and l_{spcorr} are local model parameters, $R_{\mathrm{w}j}$ and $R_{\mathrm{u}j}$ represent the DC resistances of the metal winding lines and the under-pass line, respectively. $L_{\mathrm{w}j}$ and $L_{\mathrm{u}j}$ are the self-inductances of spiral and underpass, respectively. For the layout given in Fig. 2, l_{total} can be calculated as

$$l_{\mathrm{total}} = l_{\mathrm{m}} + 2l_{\mathrm{fd}}. \tag{25}$$

The proximity effect may be considered simultaneously by introducing the mutual inductances, M_{i12}, M_{i13}, and M_{i23} between the three different inductances $L_{\mathrm{sp}ij}$ ($i = 1, 2$; $j = 1, 2, 3$).

These are calculated with mutual coefficients K_{i12}, K_{i13}, and K_{i23}, ($i = 1, 2$) which are obtained by empirical method.

$$K_{i12} = \min\left[0.99, \frac{M_{i12}}{\sqrt{L_{\mathrm{sp}i2}L_{\mathrm{sp}i1}}}\right],\quad i = 1,2, \tag{26}$$

$$K_{i13} = \min\left[0.99, \frac{M_{i13}}{\sqrt{L_{\mathrm{sp}i3}L_{\mathrm{sp}i1}}}\right],\quad i = 1,2, \tag{27}$$

$$K_{i23} = \min\left[0.99, \frac{M_{i23}}{\sqrt{L_{\mathrm{sp}i3}L_{\mathrm{sp}i2}}}\right],\quad i = 1,2. \tag{28}$$

2.4.2. DC inductance and resistance: L_{si} and R_{si} ($i = 1, 2$)

The DC resistance R_{dc} of a spiral inductor can be calculated as

$$R_{\mathrm{dc}} = R_{\mathrm{UD}}\frac{l_{\mathrm{up}}}{W_{\mathrm{U}}} + R_{\mathrm{TP}}\frac{l_{\mathrm{total}}}{W_{\mathrm{S}}}. \tag{29}$$

The distributed DC inductance L_{dc} of a spiral inductor can be calculated using Ref. [22] as follows,

$$L_{\mathrm{dc}} = \beta D_{\mathrm{out}}^{\alpha_1} W_{\mathrm{S}}^{\alpha_2} d_{\mathrm{avg}}^{\alpha_3} N^{\alpha_4} S^{\alpha_5}, \tag{30}$$

where α_i ($i = 1, 2, 3, 4, 5$) and β are layout dependent coefficients. For octagonal inductors, α_i ($i = 1, 2, 3, 4, 5$) and β are –1.21, –0.163, 2.43, 1.75, –0.149 and 1.33×10^{-3}, respectively. The average diameter d_{avg} is defined as

$$d_{\mathrm{avg}} = \frac{1}{2}(D_{\mathrm{in}} + D_{\mathrm{out}}). \tag{31}$$

As the partition method used in Eqs. (3)–(5) for the skin and proximity effects modeling is experiential, this method causes differences between the total resistance of the resistances $R_{\mathrm{sp}ij}$, ($i = 1, 2$; $j = 1, 2, 3$) and the DC resistance calculated by Eq. (29) and between the total inductance of the inductances $L_{\mathrm{sp}ij}$, ($i = 1, 2$; $j = 1, 2, 3$) and the DC inductance calculated by Eq. (30) directly. L_{si} and R_{si} are introduced to account for this. The following gives the calculation method of $L_{\mathrm{s}i}$ and R_{si}.

$$L_{si} = \frac{1}{2}l_{\mathrm{dccorr}}M_{\mathrm{L}}L_{\mathrm{dc}},\quad i = 1,2, \tag{32}$$

$$R_{si} = \frac{1}{2}r_{\mathrm{dccorr}}M_{\mathrm{R}}R_{\mathrm{dc}},\quad i = 1,2, \tag{33}$$

where

$$M_{\mathrm{R}} = 1 - 2\frac{R_{\mathrm{sp11}}//R_{\mathrm{sp12}}//R_{\mathrm{sp13}}}{R_{\mathrm{dc}}} = 1 - 2\frac{R_{\mathrm{sp11}}R_{\mathrm{sp12}}R_{\mathrm{sp13}}}{R_{\mathrm{dc}}\left(R_{\mathrm{sp12}}R_{\mathrm{sp13}} + R_{\mathrm{sp11}}R_{\mathrm{sp13}} + R_{\mathrm{sp11}}R_{\mathrm{sp12}}\right)}, \tag{34}$$

$$M_{\mathrm{L}} = 1 - 2\frac{L_{\mathrm{sp11}}//L_{\mathrm{sp12}}//L_{\mathrm{sp13}}}{L_{\mathrm{dc}}} = 1 - 2\frac{L_{\mathrm{sp11}}L_{\mathrm{sp12}}L_{\mathrm{sp13}}}{L_{\mathrm{dc}}\left(L_{\mathrm{sp12}}L_{\mathrm{sp13}} + L_{\mathrm{sp11}}L_{\mathrm{sp13}} + L_{\mathrm{sp11}}L_{\mathrm{sp12}}\right)}. \tag{35}$$

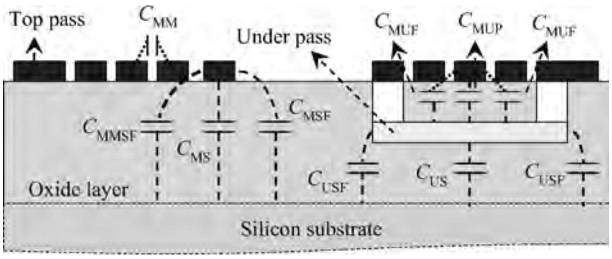

Fig. 5. Simplified schematic overview of the capacitive parasitics in an asymmetric spiral inductor. The fringing capacitances are considered.

2.4.3. Overlap and coupling capacitance: $C_p = C_{mm} + C_{mu}$

C_p represents the forward capacitance, which includes the overlap capacitance C_{mu} and the coupling capacitance C_{mm} between the neighboring segments. A simplified schematic overview of the capacitive parasitics in an asymmetric spiral inductor is illustrated in Fig. 5. Considering the parallel-plate capacitance and the fringing capacitance from spiral turn to under pass, the overlap capacitance including the fringing effect can be calculated as follows,

$$C_{mu} = c_{pcorr}\left[W_U N\left(C_{MU} W_s + 2C_{MUF}\right)\right]. \qquad (36)$$

The coupling capacitance between the neighboring turns is calculated as follows,

$$C_{mm} = c_{pcorr} C_{MM} l_{sp}, \qquad (37)$$

where c_{pcorr} is a local model parameter, and l_{sp} is the length of turn spacing.

2.4.4. Metal–oxide capacitance: C_{oxij}

The metal–oxide capacitances C_{ox11}, C_{ox12}, C_{ox21} and C_{ox22} are defined as follows,

$$C_{ox1j} = c_{oxcorr1j}\left[\frac{1}{2}\left(C_{msp} + C_{msf}\right) + C_{usp} + C_{usf}\right], \quad j = 1, 2, \qquad (38)$$

$$C_{ox2j} = \frac{1}{2} c_{oxcorr2j}\left(C_{msp} + C_{msf}\right), \quad j = 1, 2, \qquad (39)$$

where C_{msp} and C_{msf} represent the parallel-plate capacitance and the fringing capacitance from the top pass to substrate, respectively. C_{mup} and C_{muf} are the parallel-plate capacitance and the fringing capacitance from the under pass to the substrate, respectively. C_{msp}, C_{msf}, C_{mup} and C_{muf} are defined as follows,

$$C_{msp} = C_{MS} l_{total} W, \qquad (40)$$

$$C_{usp} = C_{US} l_{up} W_U, \qquad (41)$$

$$C_{msf} = 2C_{MMSF} l_m + 4C_{MSF} l_{fd} + \left(C_{MSF} - C_{MMSF}\right)\left(l_{inner} + l_{outer}\right), \qquad (42)$$

$$C_{usf} = 2 l_{up} C_{USF}, \qquad (43)$$

where l_{inner} and l_{outer} are the length of the inner and outer spiral turn, respectively. $c_{oxcorrij}$ ($i = 1, 2$; $j = 1, 2$) are local model parameters. $c_{oxcorr12} = c_{oxcorr21}$ is used in this work.

2.4.5. The vertical substrate loss model: R_{subij} and C_{subij}

The displacement current loss that resulted from the capacitive coupling effect of the silicon substrate is highly dependent on the process parameters and operating frequency. For multi-turn inductors, due to the fringing electric field of the neighboring metal segments[23], the electric field of the embedded turns is much smaller than that of the outer turn, inner turn and the feed lines. Consequently, the effective thicknesses of the substrate relative to the embedded turns and the inner turn/outer turn/feed lines are different. The thickness of the substrate relative to the embedded turns is much smaller than the original value T_{SUB}. A substrate effect factor γ_{sub} is defined here to take this effect into account. By using the modeling method for substrate capacitive and resistive coupling effects proposed in Refs. [24, 25], the substrate capacitance and conductance of the embedded turns per unit-length can be calculated by

$$C_{sub\_e} = \varepsilon_0 \varepsilon_{eff\_e} \Big/ \left\{\frac{1}{2\pi}\ln\left[8h_{r\_e} + 1/(4h_{r\_e})\right]\right\}, \qquad (44)$$

$$G_{sub\_e} = \frac{\pi\sigma_{sub}}{\ln\left[8h_{r\_e} + 1/(4h_{r\_e})\right]}\left[1 + \left(1 + 10h_{r\_e}\right)^{-1/2}\right], \qquad (45)$$

where σ_{sub} is the conductivity of substrate. h_{r_e} is the ratio of the effective thickness of the substrate relative to the embedded turns to the width of spiral turn. ε_{sub} and ε_{eff_e} are the dielectric constant and the effective dielectric constant of the substrate, respectively. σ_{sub}, h_{r_e} and ε_{eff_e} are defined as follows,

$$\sigma_{sub} = 1/R_{SUB}, \qquad (46)$$

$$h_{r\_e} = \gamma_{sub} T_{SUB}/W_S, \qquad (47)$$

$$\varepsilon_{eff\_e} = \frac{1}{2}\left[\left(\varepsilon_{sub} + 1\right) + \frac{\varepsilon_{sub} - 1}{\sqrt{1 + 10h_{r\_e}}}\right]. \qquad (48)$$

The substrate capacitance and the conductance of the inner turn, the outer turn and the feed lines per unit-length can be calculated as follows,

$$C_{sub\_o} = \varepsilon_0 \varepsilon_{eff\_o} \Big/ \left\{\frac{1}{2\pi}\ln\left[8h_{r\_o} + 1/(4h_{r\_o})\right]\right\}, \qquad (49)$$

$$G_{sub\_o} = \frac{\pi\sigma_{sub}}{\ln\left[8h_{r\_o} + 1/(4h_{r\_o})\right]_o}\left[1 + \left(1 + 10h_{r\_o}\right)^{-1/2}\right], \qquad (50)$$

where h_{r_o} is the ratio of the thickness of the substrate to the width of spiral turn, ε_{eff_o} is the dielectric constant of substrate respectively. h_{r_o} and ε_{eff_o} are defined as

$$h_{r\_o} = T_{SUB}/W_S, \qquad (51)$$

$$\varepsilon_{eff\_o} = \frac{1}{2}\left[\left(\varepsilon_{sub} + 1\right) + \frac{\varepsilon_{sub} - 1}{\sqrt{1 + 10h_{r\_o}}}\right]. \qquad (52)$$

The vertical substrate capacitance C_{subij} and resistance R_{subij}, ($i = 1, 2$; $j = 1, 2$) are calculated by

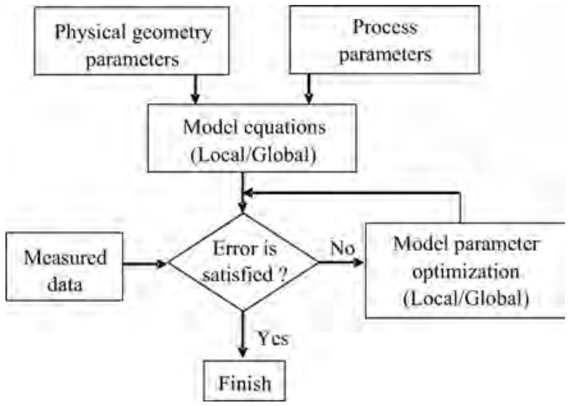

Fig. 6. Local/Global model extraction flow.

$$C_{\mathrm{sub}ij} = \frac{c_{\mathrm{subcorr}ij}}{2}\left[l_{\mathrm{m}}\left(1 - l_{\mathrm{ratio}}\right) C_{\mathrm{sub\_e}} + \left(l_{\mathrm{m}} l_{\mathrm{ratio}} + 2 l_{\mathrm{fd}}\right) \times C_{\mathrm{sub\_o}}\right], \quad i = 1,2; j = 1,2, \tag{53}$$

$$R_{\mathrm{sub}ij} = 2 r_{\mathrm{subcorr}ij}\left[l_{\mathrm{m}}\left(1 - l_{\mathrm{ratio}}\right) G_{\mathrm{sub\_e}} + \left(l_{\mathrm{m}} l_{\mathrm{ratio}} + 2 l_{\mathrm{fd}}\right) \times G_{\mathrm{sub\_o}}\right]^{-1}, \quad i = 1,2; j = 1,2, \tag{54}$$

where l_{ratio} is defined as $l_{\mathrm{ratio}} = (l_{\mathrm{inner}} + l_{\mathrm{outer}}/l_{\mathrm{m}})$, γ_{sub}, $r_{\mathrm{subcorr}ij}$ and $c_{\mathrm{subcorr}ij}$ (i =1, 2; j = 1, 2) are local model parameters. For single or half turn spiral inductors, the calculation of Eqs. (51)–(54) can be omitted.

2.4.6. The lateral substrate loss model: $R_{\mathrm{loss}i}$ and $L_{\mathrm{loss}i}$

As the eddy current is generally flowing in the lateral direction in the substrate, the eddy current effect can be taken as the major mechanism of the lateral substrate losses for spiral inductors manufactured in a specified process. For compact modeling, the concept of a complex effective thickness[18] of the substrate is introduced to determine the lateral resistances and inductances, $R_{\mathrm{loss}i}$ and $L_{\mathrm{loss}i}$ in this work.

The complex effective thickness of the substrate in which the eddy current is flowing can be defined as,

$$h_{\mathrm{eff}} = T_{\mathrm{OX}} + \frac{\delta}{2}(1 - j)\coth\left[\frac{T_{\mathrm{SUB}}}{\delta}(1 + j)\right], \tag{55}$$

where T_{OX} and T_{SUB} are the thicknesses of oxide layer and the silicon substrate, respectively. δ is defined as the skin depth of substrate at $f_{\max}$, which is calculated by

$$\delta = \frac{1}{\sqrt{\pi f_{\max}\mu_{si}\sigma_{si}}}, \tag{56}$$

where μ_{si} and σ_{si} are the permeability and conductivity of the silicon substrate, respectively.

According to the method introduced in Ref. [26], the per-unit-length series impedance of the substrate with δ is calculated as follows,

$$L^{*}(\omega) = \frac{\mu_0}{4\pi}\ln\left\{1 + 32\left(\frac{h_{\mathrm{eff}}}{W_{\mathrm{S}}}\right)^2\left[1 + \sqrt{1 + \left(\frac{\pi W_{\mathrm{S}}}{8 h_{\mathrm{eff}}}\right)^2}\right]\right\}. \tag{57}$$

By using the real and imaginary part of Eq. (57), $R_{\mathrm{loss}i}$ and $L_{\mathrm{loss}i}$ are determined by

$$R_{\mathrm{loss}i} = -l_{\mathrm{loss}i} l_{\mathrm{total}}\frac{\omega}{2}\mathrm{Im}L^{*}(\omega), \quad i = 1,2, \tag{58}$$

$$L_{\mathrm{loss}i} = \frac{1}{2} r_{\mathrm{loss}i} l_{\mathrm{total}}\mathrm{Re}\left[L^{*}(\omega)\right], \quad i = 1,2, \tag{59}$$

where $l_{\mathrm{loss}i}$ and $r_{\mathrm{loss}i}$ ($i = 1, 2$) are local model parameters. For compact modeling, the results of $L^{*}(\omega)$ at $\omega = 2\pi f_{\max}$ is used in this work.

In order to see the effect of the geometry on the strength of the eddy current, mutual inductances, $M_{\mathrm{lo}ij}$ (i = 1, 2; j = 1, 2, 3) calculated with the mutual coefficients $K_{\mathrm{lo}ij}$ (i = 1, 2; j = 1, 2, 3), between $L_{\mathrm{loss}i}$ and $L_{\mathrm{sp}ij}$ (i = 1, 2; j = 1, 2, 3). $K_{\mathrm{lo}ij}$ (i = 1, 2; j = 1, 2, 3) is experientially defined as

$$K_{\mathrm{lo}ij} = \min\left[0.99, \frac{L_{\mathrm{sp}ij}}{\sqrt{L_{\mathrm{sp}ij} L_{\mathrm{loss}i}}}\right], \quad i = 1,2; j = 1,2,3. \tag{60}$$

Table 4. Geometric parameters of asymmetric inductors manufactured on a standard 0.18-μm SiGe BiCMOS process with 100 Ω·cm substrate resistivity. $W_{\mathrm{u}} = W_{\mathrm{s}}$ is used for these devices.

DUT #	W_{s} (μm)	D_{in} (μm)	N	S (μm)
D1	8	80	1.5	2
D2, D3	8	120	1.5, 2.5	2
D4–D9	8	200	1.5, 2.5, 3.5, 4.5, 5.5, 6.5	2
D10, D11	8	240	1.5, 6.5	2
D12–D17	8	280	1.5, 2.5, 3.5, 4.5, 5.5, 6.5	
D18, D19	8	360	1.5, 6.5	2
D20–D25	8	400	1.5, 2.5, 3.5, 4.5, 5.5, 6.5	2
D26, D27	10	160	1.5, 2.5	2
D28–D31	10	200	1.5, 2.5, 3.5, 4.5	2
D32, D33	10	240	1.5, 6.5	2
D34–D36	10	280	1.5, 3.5, 6.5	2
D37	10	280	3.5	3
D38	10	280	3.5	4
D39–D41	10	360	1.5, 3.5, 6.5	2
D42–D44	10	400	1.5, 3.5, 6.5	2
D45, D46	15	200	1.5, 3.5	2
D47–D51	15	280	1.5, 2.5, 3.5, 4.5, 5.5	2
D52, D53	15	360	1.5, 6.5	2
D54–D56	15	400	1.5, 4.5, 5.5	2
D57	20	280	3.5	2
D58	20	400	3.5	2
D59	30	360	3.5	2

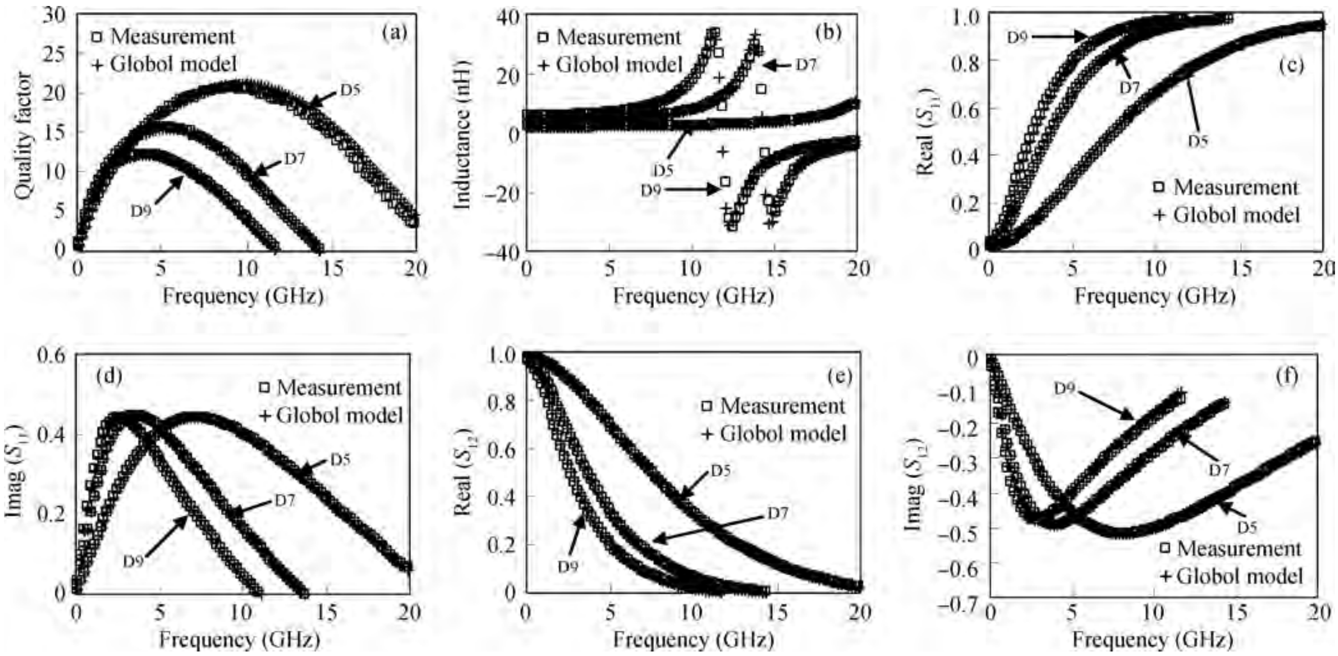

Fig. 7. Comparison between measured and double-π scalable model for asymmetric inductors with $W = 8\ \mu$m, OD = 200 μm, $S = 2\ \mu$m. (a) Quality factor. (b) Inductance. (c) Real parts of S_{11}. (d) Imagery parts of S_{11}. (e) Real parts of S_{12}. (f) Imagery parts of S_{12}.

2.5. Geometry based scaling rules and the global model

The local parameter set can be viewed as a correction of the model determined from the local model equations and the employed process and geometric parameters. The global parameters account for geometric scaling. The complete geometry scaling rules developed for the local parameter set is listed in Table 3. All the local model parameters are considered as a function of the N, D_{in} and h_{p}. h_{p} is the hollowness of an inductor with a specified geometry, which is defined as

$$h_{\text{p}} = \frac{D_{\text{in}} + W_{\text{S}}}{D_{\text{out}} - W_{\text{S}}}. \tag{61}$$

3. Model extraction and verification

A simplified global/local model extraction flowchart is given in Fig. 6. Once the process and geometry parameters required in Eqs. (1)–(47) are given (the required process parameters are generally obtained from the foundry), the local parameter set given in Table 3 can be extracted using a simple optimization procedure. The local model is then determined. For global parameter set determination, a set of measurements from inductors with different geometric parameters are required to accurately determine the global parameters given in Table 3 with an optimization procedure. Here, we choose the random optimization package and employ a HSPICE simulator as the evaluation tool for the optimization.

In order to verify the accuracy of the proposed scalable model, a set of asymmetric octagonal spiral inductors with different geometric parameters fabricated on a standard 0.18-μm SiGe BiCMOS technology are modeled using the global model proposed in this paper. The geometric parameters of these inductors are outlined in Table 4. Two-port S-parameters were measured and de-embedded (Open + Short) for parasitics introduced by the GSG PAD using an Agilent E8363B Network Analyzer and a CASCADE Summit probe station. The feed lines connected at the right and left side of the inductors are finally de-embedded from the test structures for model extraction.

Table 5. RMS errors between the global model simulated and measured inductance (L), quality factor (Q) and S-parameter of the devices listed in Table 4.

DUT	L (%)	Q (%)	S_{11} (%)		S_{12} (%)	
			real	imag	real	imag
D5	1.674	2.664	2.099	1.475	3.249	0.945
D9	1.170	2.629	1.032	1.747	5.385	3.245
D13	2.087	2.949	1.892	1.983	4.220	2.892
D21	1.940	4.164	1.625	2.121	2.487	3.643
D25	0.771	1.781	1.155	1.031	2.938	3.132
D30	2.814	3.810	2.258	1.429	3.948	1.053
D32	1.701	3.592	4.039	1.338	1.037	1.621
D36	2.465	4.388	2.325	3.707	2.405	2.634
D41	3.581	3.264	1.475	2.541	2.606	2.142
D43	2.871	3.279	1.944	3.208	1.939	2.863
D49	2.881	4.708	3.331	3.740	4.721	2.290
D53	2.260	2.776	2.833	2.964	2.206	2.200
D59	3.562	5.636	4.400	3.743	7.439	4.053

The RMS errors of the S-parameters, quality factor (Q) and inductance (L) between the measured and simulated results from the extracted global model are given in Table 5. The RMS error is defined as

$$\text{RMS\_error} = 100 \times \sqrt{\frac{1}{n}\sum_{1}^{n}\frac{(X_{\text{mea}} - X_{\text{sim}})^2}{\sum\limits_{1}^{n} X_{\text{mea}}^2/n}}, \tag{62}$$

where n is the total number of data points. The RMS error cal-

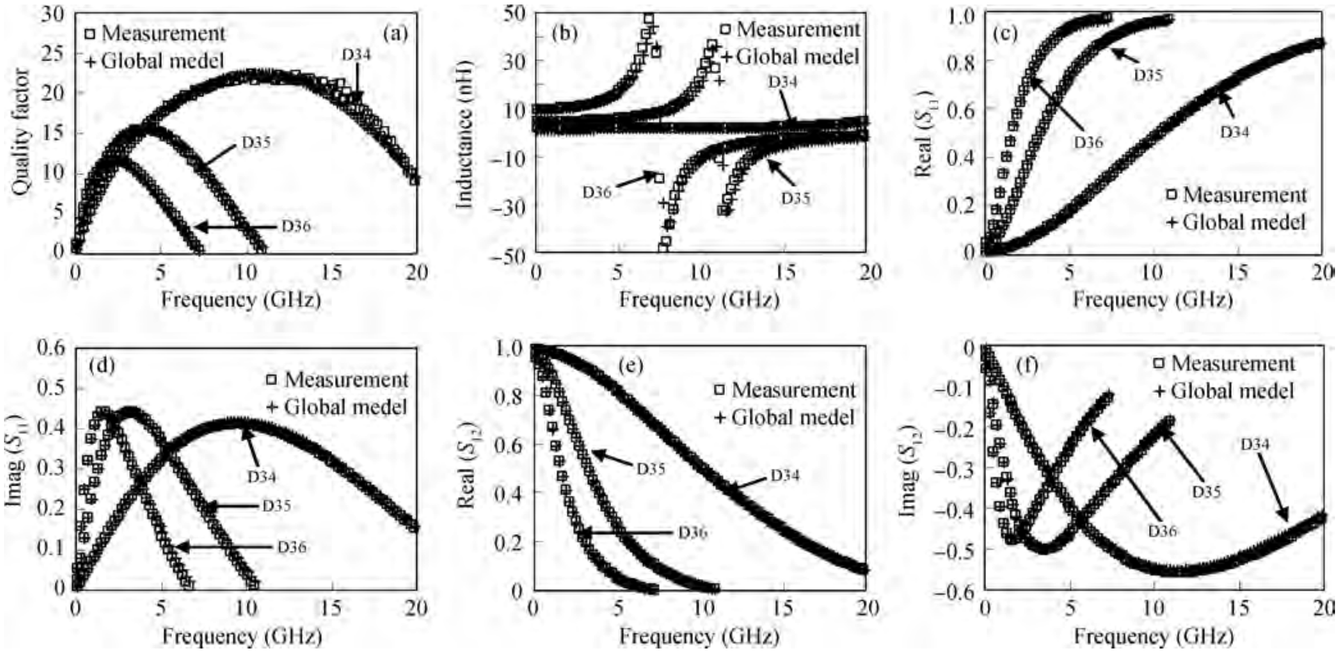

Fig. 8. Comparison between measured and double-π scalable model for asymmetric inductors with $W = 10$ μm, OD $= 280$ μm, $S = 2$ μm. (a) Quality factor. (b) Inductance. (c) Real parts of S_{11}. (d) Imagery parts of S_{11}. (e) Real parts of S_{12}. (f) Imagery parts of S_{12}.

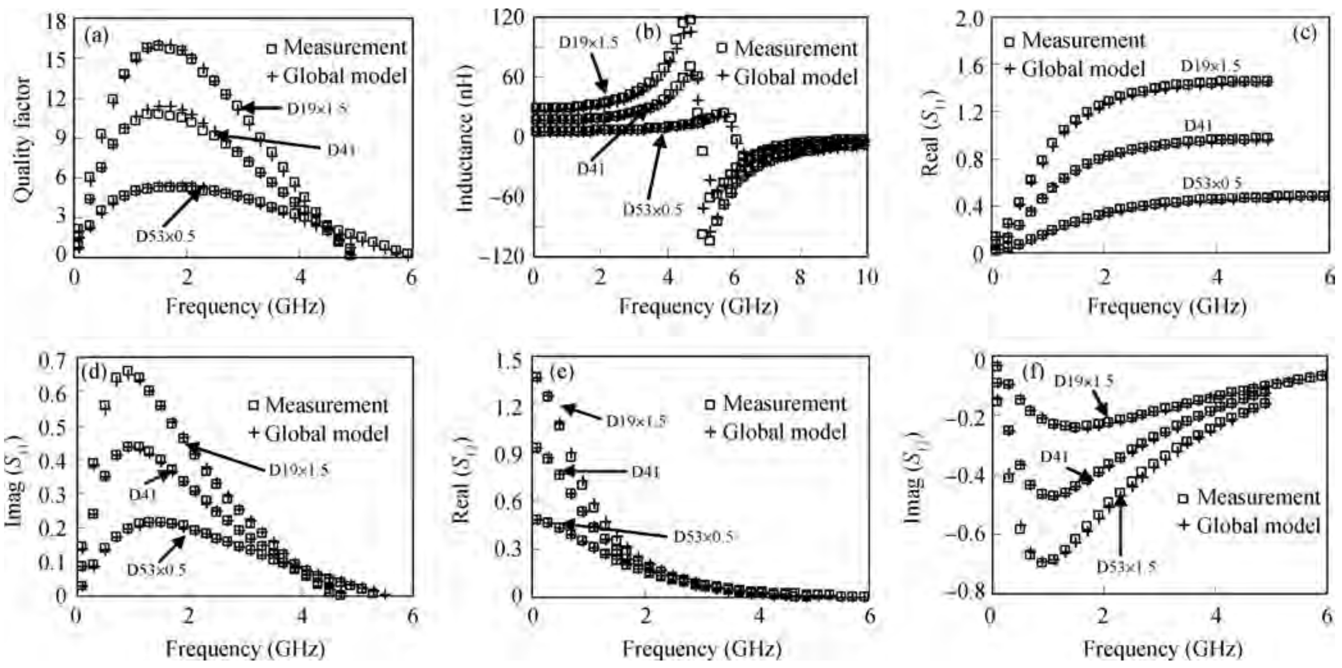

Fig. 9. Comparison between measured and double-π scalable model for asymmetric inductors with $N = 6.5$, OD $= 360$ μm, $S = 2$ μm. (a) Quality factor. (b) Inductance. (c) Real parts of S_{11}. (d) Imagery parts of S_{11}. (e) Real parts of S_{12}. (f) Imagery parts of S_{12}.

culation is executed over the frequency range from 50 MHz to the self-resonant frequency (SRF) of devices.

The measured and simulated Q, L, real(S_{11}), real(S_{12}), imag(S_{11}) and imag(S_{12}) characteristics of the asymmetric on-chip inductors, with W fixed at 8 μm, 10 μm and 15 μm, S fixed at 2 μm while changing ID and N, are shown in Figs. 7–9, respectively. The RMS errors of L between the measured and simulated data for the inductors are below 5%. The average RMS error of L is 2.291%. For most of these devices, the RMS errors of Q are below 5%, and the average error of Q is 3.511%. The average RMS errors of the real and imagery parts of S_{11} and S_{12} are 2.339%, 2.387%, 3.429% and 2.516%, respectively. The excellent agreement between the measured and simulated results verified and validated the accuracy of the proposed on-chip spiral inductor modeling technique. The accuracy of the proposed scalable rules is verified by the excellent agreement between the extracted data and scalable data of inductors with typical geometries, as shown in Fig. 10. In this picture, the extracted data of local parameters can be obtained though a optimization procedure as follows：(1) set optimization target, usually we set target to be quality factor Q, inductance L and the parasitic resistance R; (2)select the range of

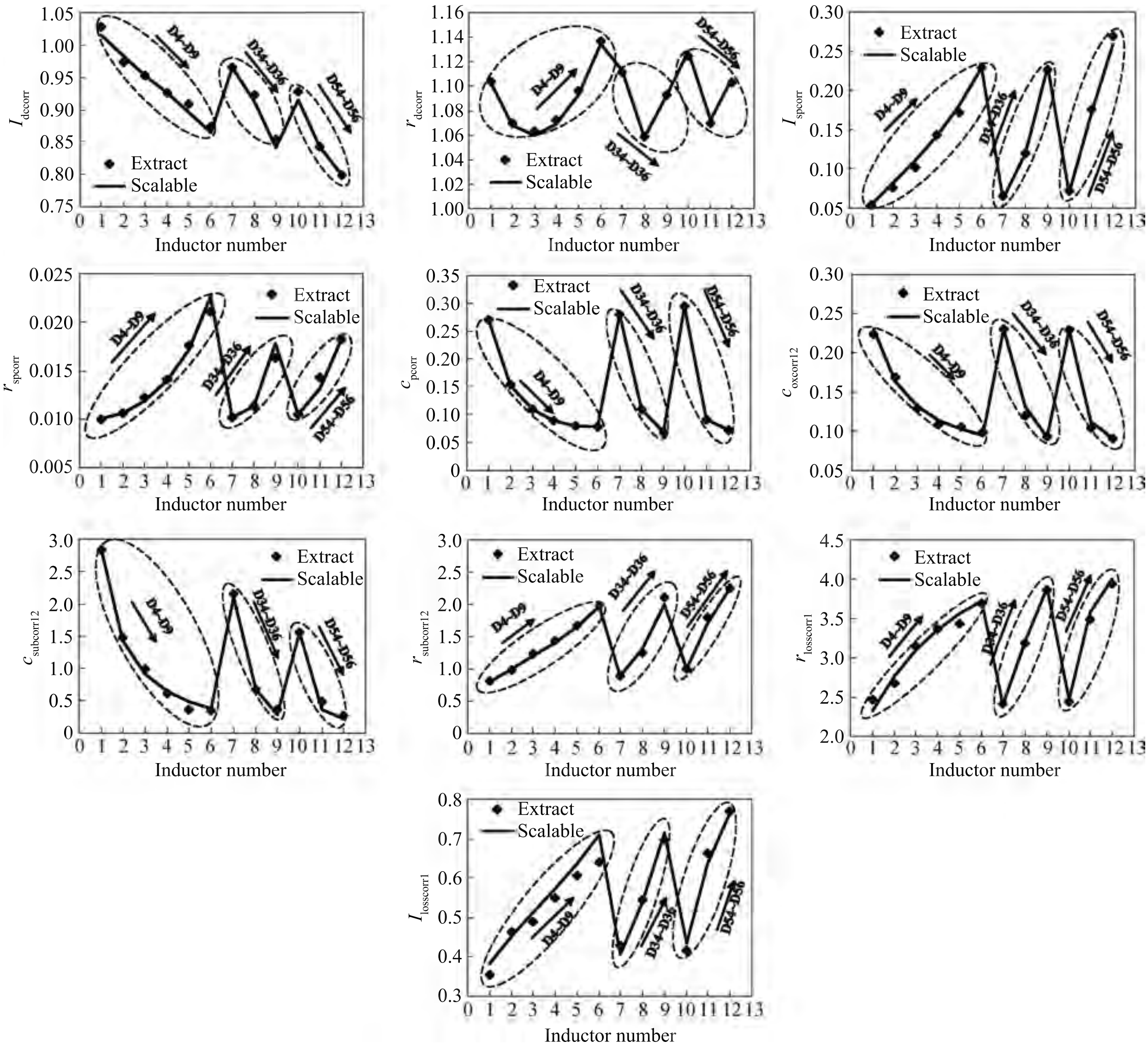

Fig. 10. Scalable data and extracted data of the model parameters.

every local parameter, the optimization algorithm and times, then start optimization. In the optimization process, we need adjust the optimization values of parameters and their range according to the geometry rules of inductors, ultimately get the best value.

4. Conclusion

An industry-oriented fully scalable compact circuit model for on-chip spiral inductors has been proposed and implemented in HSPICE. This article mainly concerns the comprehensive application of the reported literature, and obtains results to meet industrial applications. This work has not been reported in previous papers. It is very useful for circuit designers to see the scaling behavior of a model library under a defined process. The model is developed with a hierarchical structure, in which a strict partition of the geometry scaling in the global model and the model equations in the local model is defined. The major parasitic effects, including the skin effect, the proximity effect, the inductive and capacitive loss in the substrate and the distributed effect are considered and calculated using physics-based equations. Once physical-based scaling rules are determined, the model has good precision for non-sampling geometries. This has also been verified in our experiments. The accuracy of the proposed method is validated through the excellent agreement observed up to the SRF between the simulated and measured results of asymmetric inductors with different geometries fabricated by a standard 0.18-μm SiGe BiCMOS technology.

References

[1] Zhang H T, Gao H, Li G P. Broad-band power amplifier with a novel tunable output matching network. IEEE Trans Microw Theory Tech, 2005, 53(11): 3606

[2] You F, He S B, Tang X H, et al. High-efficiency single-end class-E/F_2 power amplifier with finite DC feed inductor. IEEE Trans Microw Theory Tech, 2010, 58(1): 32

[3] Entesari K, Tavakoli A R, Helmy A. CMOS distributed amplifiers with extended flat bandwidth and improved input matching using gate line with coupled inductors. IEEE Trans Microw The-

ory Tech, 2009, 57(12): 2862

[4] Kuo J J, Tsai Z M, Huang P C, et al. A wide tuning range voltage controlled oscillator using common-base configuration and inductive feedback. IEEE Microw Wireless Compon Lett, 2009, 19(10): 653

[5] Fan X, Zhang H, Sanchez-Sinencio E, et al. A noise reduction and linearity improvement technique for a differential cascode LNA. IEEE J Solid-State Circuits, 2008, 43(3): 588

[6] Guo J C, Tan T Y. A broadband and scalable model for on-chip inductors incorporating substrate and conductor loss effects. IEEE Trans Electron Devices, 2006, 53(3): 413

[7] Yue C P, Ryu C, Lau J, et al. A physical model for planar spiral inductors on silicon. IEEE IEDM Dig Tech Papers, 1996: 155

[8] Lai I C H, Fujishima M. A new on-chip substrate-coupled inductor model implemented with scalable expressions. IEEE J Solid-State Circuits, 2006, 41(11): 2491

[9] Scuderi A, Biondi T, Ragonese E, et al. A lumped scalable model for silicon integrated spiral inductors. IEEE Trans Circuits Syst, 2004, 51(6): 1203

[10] Salimy S, Toutain S, Rhallabi A, et al. An enhanced physical and scalable lumped model of RF CMOS spiral inductors. IEEE Microwave Symposium Digest, 2009: 1017

[11] Huang F Y, Jiang N, Bian E L. Modeling of single-π equivalent circuit for on-chip spiral inductors. Solid-State Electron, 2005, 49: 473

[12] Kang M, Gil J, Shin H. A simple parameter extraction method of spiral on-chip inductors. IEEE Trans Electron Devices, 2005, 52(9): 3267

[13] Gao W, Yu Z. Scalable compact circuit model and synthesis for RF CMOS spiral inductors. IEEE Trans Microw Theory Tech, 2006, 54(3): 1055

[14] Blaschke V, Victory J. A scalable model methodology for octagonal differential and single-ended inductors. IEEE Custom Integrated Circuit Conference, 2006: 717

[15] Kim S K, Kim B S. Scalable modeling of spiral inductor in 0.13 μm RF CMOS process. SoC Design Conference, 2008, 1: 437

[16] Ahn Y G, Kim S K, Chun J H, et al. Efficient scalable modeling of double-π equivalent circuit for on-chip spiral inductors. IEEE Trans Microw Theory Tech, 2009, 57(10): 2289

[17] Huang F, Lu J, Jiang N, et al. Frequency-independent asymmetric double-π equivalent circuit for on-chip spiral inductors: physics-based modeling and parameter extraction. IEEE J Solid-State Circuits, 2006, 41(10): 2272

[18] Watson A C, Melendy D, Francis P, et al. A comprehensive compact-modeling methodology for spiral inductors in silicon-based RFICs. IEEE Trans Microw Theory Tech, 2004, 52(3): 849

[19] Wang C, Liao H, Li C, et al. A wideband predictive 'double-π' equivalent-circuit model for on-chip spiral inductors. IEEE Trans Electron Devices, 2009, 56(4): 609

[20] Zou Huanhuan, Sun Lingling, Wen Jincai, et al. Scalable modeling and comparison for spiral inductors using enhanced 1-π and 2-π topologies. Journal of Semiconductors, 2010, 31(5): 055011

[21] Mei S, Ismail Y I. Modeling skin and proximity effects with reduced realizable RL circuits. IEEE Trans VLSI Syst, 2004, 12(4): 437

[22] Mohan S S, del Mar Hershenson M, Boyd S P, et al. Simple accurate expressions for planar spiral inductances. IEEE J Solid-State Circuits,1999, 34(10): 1419

[23] Schneider M V. Microstrip lines for microwave integrated circuits. Bell Syst Tech J, 1969, 48(5): 1421

[24] Hasegawa H, Furukawa M, Yanai H. Properties of microstrip lines on Si–SiO_2 system. IEEE Trans Microw Theory Tech, 1971, 19(11): 869

[25] Eo Y, Eisenstadt W R. High-speed VLSI interconnect modeling basedon S-parameter measurements. IEEE Trans Compon, Hybrids and Manufacturing Tech, 1993,16(5): 555

[26] Weisshaar A, Luoh A. Closed-form expressions for the series impedance parameters of on-chip interconnects on multilayer silicon substrates. IEEE Trans Advanced Packaging, 2004, 27(1): 126